GSA Data Repository Item 2019345

Park, Y., Swanson-Hysell, N.L., MacLennan, S.A., Maloof, A.C., Gebreslassie, M., Tremblay, M.M., Schoene, B., Alene, M., Anttila, E.S.C., Tesema, T., and Haileab, B., 2019, The lead-up to the Sturtian Snowball Earth: Neoproterozoic chemostratigraphy time-calibrated by the Tambien Group of Ethiopia: GSA Bulletin, https://doi.org/10.1130/B35178.1.

Data Repository

This document accompanies the discussion contained in the main text. All the Python code used for this study, as well as the associated data tables not included in this document, can be found at: https://github.com/Swanson-Hysell-Group/2019 Tambien Group.

Data Repository for "The lead-up to the Sturtian Snowball Earth: Neoproterozoic chemostratigraphy time-calibrated by the Tambien Group of Ethiopia"

Yuem Park[1], Nicholas L. Swanson-Hysell[1], Scott A. MacLennan[2], Adam C. Maloof[2], Mulubrhan Gebreslassie[3,4], Marissa M. Tremblay[1,5], Blair Schoene[2], Mulugeta Alene[3], Eliel S. C. Anttila[1,6], Tadele Tesema[3], Bereket Haileab[7]

[1] Department of Earth and Planetary Science, University of California, Berkeley, CA, USA

[2] Department of Geosciences, Princeton University, Princeton, NJ, USA

[3] School of Earth Sciences, Addis Ababa University, Addis Ababa, Ethiopia

[4] Current affiliation: Department of Applied Geology, Adama Science and Technology University, Adama, Ethiopia

[5] Current affiliation: Department of Earth, Atmospheric, and Planetary Sciences, Purdue University, West Lafayette, IN, USA

[6] Current affiliation: Department of Earth Science, University of California, Santa Barbara, CA, USA

[7] Department of Geology, Carleton College, Northfield, MN, USA

This document accompanies the discussion contained in the main text. All the Python code used for this study, as well as the associated data tables not included in this document, can be found at https://github.com/Swanson-Hysell-Group/2019_Tambien_Group. A release of this GitHub repository was also made and published at https://doi.org/10.5281/zenodo.3403180.

Construction of the Chemostratigraphic Composite

The main text contains a composite $\delta^{13}C$ and $^{87}Sr/^{86}Sr$ curves for the Tonian and Cryogenian that are time-calibrated by the record from Ethiopia and incorporate data from the literature from numerous sources. Additional details associated with the data sets within this composite are provided below. The Python code used to develop the composite as well as the associated data table can be found at: https://github.com/Swanson-Hysell-Group/2019_Tambien_Group.

Ethiopia

$\delta^{13}C$ and $^{87}Sr/^{86}Sr$ data from Ethiopia comes from the Tambien Group and are developed in Miller et al. (2009), Swanson-Hysell et al. (2015b), and this study. Combined with U-Pb ID-TIMS dates on zircons from Swanson-Hysell et al. (2015b) (815.29±0.32, 788.72±0.24, and 787.38±0.14 Ma) and new U-Pb ID-TIMS dates on zircons from MacLennan et al. (2018) (735.25±0.25, 719.58±0.56, and 719.68±0.46 Ma), the Tambien Group is now the source of the most temporally well-constrained pre-Sturtian chemostratigraphic dataset to date. We therefore use the Tambien Group $\delta^{13}C$ curve as the backbone for making correlations with other datasets. In the chemostratigraphic composite, the age of the initiation of the Sturtian Glaciation is set to 717 Ma (discussed further in the 'Onset of the Sturtian Snowball' section).

Svalbard

$\delta^{13}C$ and $^{87}Sr/^{86}Sr$ data from Svalbard come from the Akademikerbreen Group and are developed in Halverson et al. (2007a) and Halverson et al. (2007b). However, a slightly stricter threshold for $^{87}Sr/^{86}Sr$ diagenesis is applied to the data included in our composite than in the original publication ([Sr]<500 ppm). Additional $^{87}Sr/^{86}Sr$ data were published in Cox et al. (2016). The Polarisbreen Group, which unconformably overlies the Akademikerbreen Group, contains two separate diamictite units which have been interpreted to represent the Sturtian and Marinoan

Glaciations respectively (Halverson et al., 2004). This correlation constrains the Akademikerbreen Group to have been deposited prior to the Sturtian Glaciation. No direct geochronological constraints exist for the Akademikerbreen Group although thermal subsidence models have been used to suggest a ca. 800 Ma age for the Bitter Springs stage (Maloof et al., 2006). Therefore, the $\delta^{13}C$ curve from the group is correlated to that of the Tambien Group by aligning the start and end of the Bitter Springs stage and the nadir of the 735 Ma Anomaly. This correlation results in a near constant sedimentation rate between these constraints, which is used to estimate the age of data that precedes the Bitter Springs stage.

Greenland

$\delta^{13}C$ and $^{87}Sr/^{86}Sr$ data from the Eleanore Bay Supergroup are developed in Cox et al. (2016). Halverson et al. (2004) approximated the age of the this succession to be ca. 800 Ma based on the correlation of lithological and $\delta^{13}C$ data to the Akademikerbreen Group of Svalbard, but no direct age constraints exist. Therefore, the age model is estimated based on aligning the $\delta^{13}C$ data with the $\delta^{13}C$ curve of the Akademikerbreen Group.

Australia

$\delta^{13}C$ data from the Bitter Springs Formation are developed in Swanson-Hysell et al. (2010). Further $^{87}Sr/^{86}Sr$ data are developed in Cox et al. (2016). Similar to the Akademikerbreen Group, the Bitter Springs Formation is unconformably overlain by Sturtian diamictite of the Areyonga Formation (Swanson-Hysell et al., 2010), and thus constrains the Bitter Springs Formation to have been deposited prior to the Sturtian Glaciation. However, no direct geochronological constraints exist for the Bitter Springs Formation. Therefore, the $\delta^{13}C$ curve from this group is correlated to that of the Tambien Group by aligning the start and end of the Bitter Springs stage. Again, this correlation results in a near constant sedimentation rate between these constraints, which is used to estimate the age of data that post-dates the Bitter Springs

stage. However, if the constant sedimentation rate is applied to $\delta^{13}C$ data from the Bitter Springs Formation preceding the Bitter Springs stage, there is a significant mismatch between these data and that of the Akademikerbreen Group. Therefore, these data were assigned slightly older ages than would be predicted by the constant sedimentation rate assumption in order to better match the $\delta^{13}C$ curves between these two sections.

Canada

$\delta^{13}C$ and $^{87}Sr/^{86}Sr$ data from Canada come from multiple studies and localities.

$\delta^{13}C$ data and geochronology from the Fifteenmile Group are developed in Macdonald et al. (2010). Additional $^{87}Sr/^{86}Sr$ data are developed in Cox et al. (2016). The Fifteenmile Group is unconformably overlain by temporally well-constrained (see the 'Onset of the Sturtian Snowball' section) Sturtian diamictite of the Upper Mount Harper Group (Macdonald et al., 2010). A U-Pb ID-TIMS date on zircons within a tuff of 811.51±0.25 Ma can be tied directly to this curve, and, combined with dates from the Tambien Group (787.38±0.14, 788.72±0.24, and 815.29±0.32 Ma), suggests global synchroneity of the Bitter Springs stage (Swanson-Hysell et al., 2015b). The nadir of the 735 Ma Anomaly can also be easily identified and correlated. Furthermore, $\delta^{13}C$ data that precede the Bitter Springs stage correlate well with data from the Akademikerbeen Group, and thus were correlated based on similar $\delta^{13}C$ values. However, unlike other sections in which the Bitter Springs stage is observed, the recovery from the interval of low $\delta^{13}C$ values appears to be much more gradual. Nevertheless, the end of the minimum $\delta^{13}C$ values is assumed to be correlative to the end of the Bitter Springs stage, and a roughly constant sedimentation rate was applied to the data between this age and the 735 Ma Anomaly nadir, excluding an unconformity interpreted to exist between PF1 and PF3 of the Fifteenmile Group (Macdonald et al., 2010).

$\delta^{13}C$ and $^{87}Sr/^{86}Sr$ data from the Little Dal Group are developed in Halverson (2006) and Halverson et al. (2007a). A slightly stricter threshold for $^{87}Sr/^{86}Sr$ diagenesis is applied to the data included in our composite ([Sr]<250 ppm and Mn/Sr>0.15) than in the original work. A

basalt has been interpreted to conformably overlie the Little Dal Group (Aitken, 1981) and inferred to have erupted ca. 780 Ma based on geochemical similarity to mafic dikes and sills that intrude the Mackenzie Mountain Supergroup (Harlan et al., 2003). Given that the basalt has not been directly dated, there is some uncertainty associated with this interpretation. Nevertheless, correlating the $\delta^{13}C$ curve from the Little Dal Group to that of the Tambien Group by aligning the start and end of the Bitter Springs stage and assuming constant sedimentation rate throughout the rest of the section suggests that the top of the Little Dal Group is ca. 780 Ma, consistent with the inference of Harlan et al. (2003).

$\delta^{13}C$ and $^{87}Sr/^{86}Sr$ data and geochronology from the Coates Lake Group are developed in Halverson (2006), Halverson et al. (2007a), and Rooney et al. (2014). A Re-Os isochron date on black shales of 732.2±3.9 Ma can be tied directly to this curve as it comes from strata recording the recovery from the nadir of the 735 Ma $\delta^{13}C$ Anomaly. This date provides constraints on the temporal alignment of the curve. Given the uncertainty associated with the date, the correlation is further refined by aligning the nadir and recovery of the excursion with the Tambien Group data.

$\delta^{13}C$ and $^{87}Sr/^{86}Sr$ data from the Shaler Supergroup are developed in Asmerom et al. (1991), although $^{87}Sr/^{86}Sr$ data with Mn/Sr>3 and $\delta^{18}O$ <-10‰ are considered to be altered. Further $\delta^{13}C$ data are developed in Jones et al. (2010). Age constraints on these strata are poor. However, the onset of the Bitter Springs Anomaly and the 735 Ma Anomaly as well as other minor inflexions in the $\delta^{13}C$ curve are identifiable in the data. Furthermore, lithostratigraphic correlations between the Shaler Supergroup and the Mackenzie Mountains Supergroup can be made. Therefore, the age model for these data is developed based on the correlation of the $\delta^{13}C$ curve as well as the lithostratigraphy between these two supergroups, as in Jones et al. (2010).

Scotland

$\delta^{13}C$ and $^{87}Sr/^{86}Sr$ data from the Dalradian Supergroup are developed in Sawaki et al. (2010). The carbonates from which these data are sourced unconformably underlie a glacial diamictite.

Brasier et al. (2000) argues that $^{87}Sr/^{86}Sr$ values from these carbonates are too low (<0.7065) to be post-Sturtian, and therefore must be pre-Sturtian in age. Besides this argument, no direct geochronological constraints exist for the Dalradian Supergroup. Therefore, the $\delta^{13}C$ curve from this group is correlated to that of the Tambien Group by aligning the nadir of the 735 Ma Anomaly.

Russia

$\delta^{13}C$ and $^{87}Sr/^{86}Sr$ data from Siberia come from multiple sources.

$\delta^{13}C$ and $^{87}Sr/^{86}Sr$ data from the Proterozoic carbonates of the UchurMaya and Turukhansk regions of Siberia are developed in Bartley et al. (2001), with additional $^{87}Sr/^{86}Sr$ data from Cox et al. (2016). All available $^{87}Sr/^{86}Sr$ data from Bartley et al. (2001) had [Sr]<500 ppm, and as a result Mn/Sr>0.5 is the only threshold applied for diagenesis. Age constraints on these strata are poor. Therefore, the age model applied to these data was based on lithostratigraphic correlation to the Yenisey Ridge and Uchur Maya Region sections, which are temporally constrained to have been deposited ca. 1100-1000 Ma based on geochronological constraints of varying robustness (Gallet et al., 2012).

$\delta^{13}C$ and $^{87}Sr/^{86}Sr$ data from the Karatau Group of the Urals are developed in Kuznetsov et al. (2006), with additional $^{87}Sr/^{86}Sr$ data from (Cox et al., 2016). However, a slightly stricter threshold for $^{87}Sr/^{86}Sr$ diagenesis was applied to the data included in our composite ([Sr]<350 ppm and Mn/Sr>0.1). Correlation of microbiota across Siberia suggests that the group is younger than ca. 1030 Ma (Kuznetsov et al., 2006). However, no other direct age control is available for this group. Therefore, following Cox et al. (2016), the age model for the Karatau Group data is constructed based on the correlation of one ca. 970 Ma Turukhansk Uplift $^{87}Sr/^{86}Sr$ measurement to the start of the Karatau Group data.

Cryogenian Successions

Since Tambien Group chemostratigraphy is limited to the Tonian, our Cryogenian $\delta^{13}C$ and $^{87}Sr/^{86}Sr$ chemostratigraphic composite is a compilation of a number of other Cryogenian datasets. In general, correlations between datasets are made using absolute age constraints where possible - otherwise, characteristic negative $\delta^{13}C$ excursions (the ca. 659 Ma Rasthof Excursion, the ca. 655 Ma Taishir Anomaly, and the ca. 643 Ma Trezona Anomaly) are used to align datasets. Unless mentioned otherwise, the same criteria for diagenesis that were used for publication of the original datasets are applied here.

Mongolia

$\delta^{13}C$ and $^{87}Sr/^{86}Sr$ data from Mongolia come from the Tsagaan-Olam Group and are developed in Bold et al. (2016) and Brasier et al. (1996). Given that data from this group span the entirety of the Cryogenian and into the Ediacaran, we use it as the backbone for our Cryogenian composite. For both datasets we apply a [Sr]<500 ppm and Mn/Sr>0.3 threshold for $^{87}Sr/^{86}Sr$ diagenesis.

The age model for these data follows that of Bold et al. (2016). A minimum age for the end of the Sturtian Glaciation is constrained by the following: U-Pb ID-TIMS on zircon from a tuffaceous bed overlying Sturtian diamicite in south China yields an age of 662.9±4.3 Ma (Zhou et al., 2004), a Re-Os isochron on black shales overlying Sturtian diamictite in northwest Canada yields an age of 662.4±4.6 Ma (Rooney et al., 2014), and a Re-Os isochron on black shales overlying Sturtian diamictite in Mongolia yields an age of 659.0±4.5 Ma (Rooney et al., 2015). A maximum age for the end of the Sturtian Glaciation is constrained by U-Pb ID-TIMS on zircon from a tuff interbedded with Sturtian diamictite in Australia, which yields an age of 663.03±0.11 Ma (Cox et al., 2018). Therefore, for our Cryogenian composite, we set the age of the end of the Sturtian Glaciation (and therefore the age of the base of the Tsagaan-Olam Group) to 660 Ma.

A maximum age for the start of the Marinoan Glaciation comes from a U-Pb SHRIMP age on zircon from a tuff underlying Marinoan diamictite in south China of 654.5±3.8 Ma (Zhang et al., 2008). However, this tuff is separated from the Marinoan diamictite by a major disconformity, and so the age for the start of the Marinoan Glaciation is likely significantly younger than this U-Pb SHRIMP age. Therefore, following Bold et al. (2016), we set the age for the start of the Marinoan Glaciation in our composite to be 640 Ma.

The end of the Marinoan Glaciation is tightly temporally constrained. Zircons from a volcanic ash within and just above Marinoan diamictite in south China yielded U-Pb ID-TIMS dates of 635.5±0.6 and 635.2±0.6 Ma respectively (Condon et al., 2005). This constraint is consistent with U-Pb ID-TIMS dates from zircon from tuffs within Marinoan diamictite of 635.5±1.2 Ma in Namibia (Hoffmann et al., 2004), and 636.4±0.5 Ma in Tasmania, Australia (Calver et al., 2013).

Canada

$\delta^{13}C$, $^{87}Sr/^{86}Sr$, and geochronological data from the Hay Creek Group are developed in Rooney et al. (2014). A Re-Os isochron on black shales from within this group yielded an age of 662.4±4.6 Ma. The $\delta^{13}C$ and $^{87}Sr/^{86}Sr$ data correlate well with that from Mongolia.

Australia

$\delta^{13}C$ data from the Amadeus Basin and Adelaide Rift Complex are taken from Swanson-Hysell et al. (2010) for the composite. Amadeus Basin data from the Bitter Springs Formation are older than the Sturtian diamictite of the Areyonga Formation which unconformably overlie it. Re-Os isochrons developed for black shales above the Areyonga Formation yielded ages of 643.0±2.4 and 657.2±5.4 Ma (Kendall et al., 2006). Data from the Etina and Trezona Formations of the Adelaide Rift Complex come from between Sturtian and Marinoan glacial deposits. It remains unclear whether or not the Taishir and Trezona Excursions are time equivalent. In this compilation, they are taken to be distinct following Bold et al. (2016) such that the Trezona Anomaly and

subsequent recovery occur temporally close to the initiation of the Marinoan Glaciation. The close temporal connection implied by this age model between the Trezona Anomaly and the initiation of the Marinoan Glaciation needs further work to be substantiated, although dropstones have been documented in the uppermost Trezona Formation (Rose et al., 2012). The data from the Adelaide Rift Complex shows that the δ^{13}C recovers from the nadir of the Trezona Anomaly over ∼200 m such that recovery from the excursion occurred prior to local ice advance (Rose et al., 2012). While this does not necessarily mean that there is a substantial separation in time between the Marinoan Glaciation and the nadir of the Trezona Anomaly, it does suggest that the δ^{13}C values recovered from the negative anomaly to values near 0‰ prior to glaciation.

Namibia

δ^{13}C and $^{87}Sr/^{86}Sr$ data from the Otavi Group are developed in Halverson et al. (2005) and Halverson et al. (2007a). We applied [Sr]<500 ppm and Mn/Sr>0.1 as the thresholds for $^{87}Sr/^{86}Sr$ alteration. Apart from the 635.5±1.2 Ma age from Hoffmann et al. (2004) constraining the end of the Marinoan Glaciation, no direct geochronological constraints exist for this data. Therefore, we align the Trezona Anomaly between the data from Australia and Namibia.

Geochronology

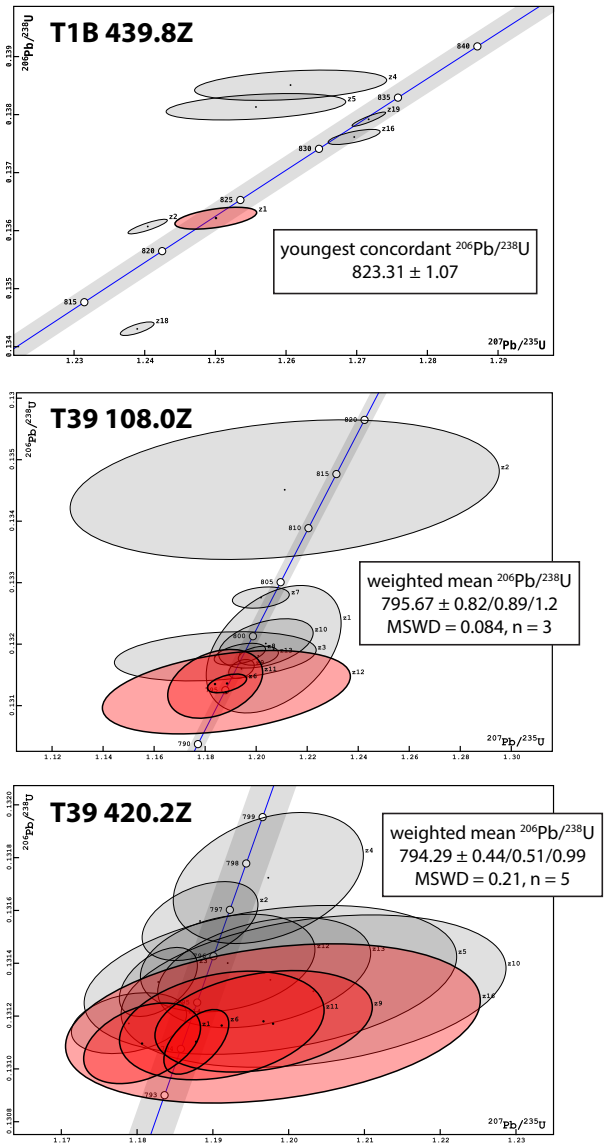

Figure DR1. Concordia diagrams for dates reported in this study. 2σ uncertainties are reported in the format ±X/Y/Z, where X is the internal (analytical) uncertainty in the absence of all external or systematic errors, Y is the uncertainty incorporating the U-Pb tracer calibration error, and Z is the uncertainty including X and Y, as well as the uranium decay constant uncertainty; MSWD = mean square of weighted deviates; n = number of zircon analyses included in the calculated date.

Table DR1. U-Pb data for analyzed zircon from T1B-439.8Z.

	Dates (Ma)								Composition				Isotopic Ratios						
	[a]		[b]		[a,b]			[c]	[d]	[e]	[f]	[g]	[h]	[a,i]		[b,i]		[a,b,i]	
fraction	$\frac{^{206}Pb}{^{238}U}$	± (2σ)	$\frac{^{207}Pb}{^{235}U}$	± (2σ)	$\frac{^{207}Pb}{^{206}Pb}$	± (2σ)	corr. coef.	% disc.	$\frac{Th}{U}$	Pb* (pg)	Pb_c (pg)	$\frac{Pb^*}{Pb_c}$	$\frac{^{206}Pb}{^{204}Pb}$	$\frac{^{206}Pb}{^{238}Pb}$	± (2σ%)	$\frac{^{207}Pb}{^{235}U}$	± (2σ%)	$\frac{^{207}Pb}{^{206}Pb}$	± (2σ%)
z1	823.31	1.07	823.43	2.61	823.76	8.55	0.51	0.10	0.34	23.13	0.61	37.96	2348.88	0.14	0.14	1.25	0.46	0.07	0.41
z2	822.49	0.71	819.07	1.26	809.80	3.20	0.85	-1.53	0.35	68.32	0.62	110.86	6810.02	0.14	0.09	1.24	0.22	0.07	0.15
z4	836.29	1.48	828.20	6.10	806.54	21.58	0.33	-3.65	0.53	13.16	0.86	15.23	908.36	0.14	0.19	1.26	1.08	0.07	1.03
z5	834.19	1.29	825.99	5.72	803.99	20.17	0.37	-3.72	0.67	13.33	0.80	16.67	958.46	0.14	0.16	1.26	1.01	0.07	0.96
z16	831.24	0.74	832.22	1.64	834.86	4.89	0.69	0.47	0.65	13.75	0.22	61.23	3610.31	0.14	0.10	1.27	0.29	0.07	0.23
z17	855.05	0.73	855.83	1.17	857.86	2.59	0.92	0.36	0.73	32.33	0.18	181.54	10466.28	0.14	0.09	1.32	0.20	0.07	0.12
z18	812.48	0.67	818.40	1.08	834.51	2.95	0.73	2.67	0.75	42.34	0.32	130.41	7480.36	0.13	0.09	1.24	0.19	0.07	0.14
z19	832.98	0.69	833.16	1.06	833.64	2.36	0.90	0.12	0.57	47.38	0.18	266.55	15958.64	0.14	0.09	1.27	0.19	0.07	0.11

Notes:
Colored rows indicate fractions included in the calculation of the reported sample age.
Isotopic dates calculated using $\lambda 238 = 1.55125 \times 10^{-10}$ and $\lambda 235 = 9.8485 \times 10^{-10}$ (Jaffey et al., 1971).
[a] Corrected for initial Th/U disequilibrium using radiogenic ^{208}Pb and Th/U[magma] = 3.50000.
[b] Corrected for initial Pa/U disequilibrium using initial fraction activity ratio $[^{231}Pa]/[^{235}U] = 1.10000$.
[c] % discordance = 100 - (100 × ($^{206}Pb/^{238}U$ date) / ($^{207}Pb/^{206}Pb$ date))
[d] Th contents calculated from radiogenic ^{208}Pb and ^{230}Th-corrected $^{206}Pb/^{238}U$ date of the sample, assuming concordance between U-Pb Th-Pb systems.
[e] Total mass of radiogenic Pb.
[f] Total mass of common Pb.
[g] Ratio of radiogenic Pb (including ^{208}Pb) to common Pb.
[h] Measured ratio corrected for fractionation and spike contribution only.
[i] Measured ratios corrected for fractionation, tracer and blank.

Table DR2. U-Pb data for analyzed zircon from T39-108.0Z.

	Dates (Ma)								Composition				Isotopic Ratios						
	[a] $\frac{^{206}Pb}{^{238}U}$	± (2σ)	[b] $\frac{^{207}Pb}{^{235}U}$	± (2σ)	[a,b] $\frac{^{207}Pb}{^{206}Pb}$	± (2σ)	corr. coef.	[c] % disc.	[d] $\frac{Th}{U}$	[e] Pb* (pg)	[f] Pb_c (pg)	[g] $\frac{Pb^*}{Pb_c}$	[h] $\frac{^{206}Pb}{^{204}Pb}$	[a,i] $\frac{^{206}Pb}{^{238}Pb}$	± (2σ%)	[b,i] $\frac{^{207}Pb}{^{235}U}$	± (2σ%)	[a,b,i] $\frac{^{207}Pb}{^{206}Pb}$	± (2σ%)
fraction																			
z1	798.88	5.90	803.74	12.16	817.26	41.88	0.41	2.29	0.57	1.59	0.25	6.29	395.48	0.13	0.79	1.21	2.19	0.07	2.00
z2	813.64	6.45	805.73	38.62	783.94	142.22	0.26	-3.75	0.56	0.54	0.30	1.78	125.78	0.13	0.84	1.21	6.94	0.07	6.77
z3	798.22	2.28	793.16	18.38	778.96	68.88	0.25	-2.43	0.51	4.01	1.13	3.54	233.74	0.13	0.30	1.18	3.34	0.07	3.28
z6	795.71	0.87	795.30	3.56	794.14	12.54	0.49	-0.16	0.47	5.66	0.27	20.81	1297.81	0.13	0.12	1.19	0.65	0.07	0.60
z7	803.66	0.98	801.43	5.14	795.22	18.90	0.27	-1.02	0.43	4.03	0.31	12.82	813.30	0.13	0.13	1.20	0.93	0.07	0.90
z8	798.42	1.01	797.63	4.66	795.41	16.56	0.46	-0.34	0.58	5.09	0.31	16.30	993.36	0.13	0.13	1.19	0.84	0.07	0.79
z9	797.04	0.88	797.93	2.31	800.40	8.21	0.36	0.46	0.73	12.47	0.33	38.31	2223.30	0.13	0.12	1.19	0.42	0.07	0.39
z10	799.42	2.28	802.34	8.53	810.47	30.06	0.42	1.40	0.50	2.01	0.20	10.01	628.68	0.13	0.30	1.20	1.54	0.07	1.44
z11	795.67	3.19	793.15	8.65	786.05	31.21	0.33	-1.18	0.44	2.11	0.27	7.93	509.16	0.13	0.43	1.18	1.57	0.07	1.49
z12	794.90	3.87	795.18	22.55	795.97	82.26	0.38	0.18	0.42	1.37	0.39	3.54	238.72	0.13	0.52	1.19	4.09	0.07	3.92
z13	798.28	0.88	800.97	3.63	808.48	13.15	0.31	1.30	0.43	5.40	0.28	19.34	1218.11	0.13	0.12	1.20	0.65	0.07	0.63

Notes:
Colored rows indicate fractions included in the calculation of the reported sample age.
Isotopic dates calculated using $\lambda 238 = 1.55125\times10^{-10}$ and $\lambda 235 = 9.8485\times10^{-10}$ (Jaffey et al., 1971).
[a] Corrected for initial Th/U disequilibrium using radiogenic ^{208}Pb and Th/U[magma] = 3.50000.
[b] Corrected for initial Pa/U disequilibrium using initial fraction activity ratio $[^{231}Pa]/[^{235}U] = 1.10000$.
[c] % discordance = 100 - (100 × ($^{206}Pb/^{238}U$ date) / ($^{207}Pb/^{206}Pb$ date))
[d] Th contents calculated from radiogenic ^{208}Pb and ^{230}Th-corrected $^{206}Pb/^{238}U$ date of the sample, assuming concordance between U-Pb Th-Pb systems.
[e] Total mass of radiogenic Pb.
[f] Total mass of common Pb.
[g] Ratio of radiogenic Pb (including ^{208}Pb) to common Pb.
[h] Measured ratio corrected for fractionation and spike contribution only.
[i] Measured ratios corrected for fractionation, tracer and blank.

Table DR3. U-Pb data for analyzed zircon from T39-420.2Z.

	Dates (Ma)								Composition				Isotopic Ratios						
fraction	$^{a}\frac{^{206}Pb}{^{238}U}$	± (2σ)	$^{b}\frac{^{207}Pb}{^{235}U}$	± (2σ)	$^{a,b}\frac{^{207}Pb}{^{206}Pb}$	± (2σ)	corr. coef.	^{c} % disc.	$^{d}\frac{Th}{U}$	^{e} Pb* (pg)	^{f} Pb$_c$ (pg)	$^{g}\frac{Pb^*}{Pb_c}$	$^{h}\frac{^{206}Pb}{^{204}Pb}$	$^{a,i}\frac{^{206}Pb}{^{238}Pb}$	± (2σ%)	$^{b,i}\frac{^{207}Pb}{^{235}U}$	± (2σ%)	$^{a,b,i}\frac{^{207}Pb}{^{206}Pb}$	± (2σ%)
z1	794.12	0.87	791.62	3.59	784.58	12.98	0.38	-1.18	0.69	11.98	0.49	24.28	1391.39	0.13	0.12	1.18	0.65	0.07	0.62
z2	796.76	0.85	795.17	3.55	790.74	12.69	0.42	-0.73	0.87	15.22	0.59	25.79	1415.45	0.13	0.11	1.19	0.64	0.07	0.60
z3	795.44	0.75	792.62	2.40	784.69	8.35	0.48	-1.33	0.76	23.62	0.59	40.01	2239.52	0.13	0.10	1.18	0.44	0.07	0.40
z4	797.69	1.41	799.35	5.80	803.97	20.92	0.34	0.82	0.73	13.69	0.91	15.02	857.80	0.13	0.19	1.20	1.05	0.07	1.00
z5	795.49	1.61	799.47	11.36	810.60	41.75	0.31	1.90	0.64	12.24	1.71	7.15	427.13	0.13	0.21	1.20	2.05	0.07	2.00
z6	794.15	0.70	794.95	1.99	797.18	6.68	0.55	0.42	0.77	43.52	0.87	50.28	2801.05	0.13	0.09	1.19	0.36	0.07	0.32
z9	794.59	1.09	799.06	6.63	811.54	24.38	0.28	2.12	1.20	8.79	0.62	14.19	731.99	0.13	0.15	1.20	1.20	0.07	1.17
z10	795.25	1.64	802.10	11.70	821.19	42.92	0.30	3.19	1.06	10.65	1.38	7.70	416.84	0.13	0.22	1.20	2.11	0.07	2.06
z11	794.51	1.17	796.51	6.26	802.10	23.04	0.28	0.98	0.69	5.42	0.40	13.43	776.60	0.13	0.16	1.19	1.13	0.07	1.10
z12	795.85	1.05	796.87	5.34	799.70	19.65	0.27	0.51	1.16	10.71	0.61	17.46	903.55	0.13	0.14	1.19	0.97	0.07	0.94
z13	795.65	1.19	799.10	6.49	808.72	23.61	0.35	1.65	0.66	5.25	0.40	13.04	760.42	0.13	0.16	1.20	1.17	0.07	1.13
z14	794.55	0.66	790.82	3.54	780.29	13.14	0.29	-1.80	1.30	10.90	0.40	27.31	1363.19	0.13	0.09	1.18	0.64	0.07	0.62
z16	794.55	1.72	799.63	12.64	813.80	46.60	0.29	2.40	0.66	7.30	1.14	6.40	382.41	0.13	0.23	1.20	2.28	0.07	2.23

Notes:
Colored rows indicate fractions included in the calculation of the reported sample age.
Isotopic dates calculated using $\lambda 238 = 1.55125\times10^{-10}$ and $\lambda 235 = 9.8485\times10^{-10}$ (Jaffey et al., 1971).
[a] Corrected for initial Th/U disequilibrium using radiogenic ^{208}Pb and Th/U[magma] = 3.50000.
[b] Corrected for initial Pa/U disequilibrium using initial fraction activity ratio $[^{231}Pa]/[^{235}U] = 1.10000$.
[c] % discordance = 100 - (100 × (^{206}Pb/^{238}U date) / (^{207}Pb/^{206}Pb date))
[d] Th contents calculated from radiogenic ^{208}Pb and ^{230}Th-corrected ^{206}Pb/^{238}U date of the sample, assuming concordance between U-Pb Th-Pb systems.
[e] Total mass of radiogenic Pb.
[f] Total mass of common Pb.
[g] Ratio of radiogenic Pb (including ^{208}Pb) to common Pb.
[h] Measured ratio corrected for fractionation and spike contribution only.
[i] Measured ratios corrected for fractionation, tracer and blank.

Figure DR2. **(A)** Photograph of the lava flow T1b-439.8Z. **(B)** Photograph of the ignimbrite T39-108.0Z, with feldspar phenocrysts and fiammed lithic clasts. **(C)** Photograph of the 30 cm rhyolitic tuff T39-420.2Z, with normally graded lapilli at the base. Hammer points up section in all panels.

Diagenetic Considerations

Isotope Conglomerate Test

We compare δ^{13}C and δ^{18}O values of the carbonate clasts from within diamictite of the Negash Formation of the Negash Syncline and Samre Fold-Thrust Belt. In general, the distribution of clast δ^{13}C values is similar to that of the *in situ* Tambien Group carbonates (Fig. DR3A). However, the filtering technique proposes that the stratigraphic distance of a sample to the closest siliciclastic unit is a reasonable predictor for δ^{13}C alteration in *in situ* Tambien Group carbonates. If such a scenario applied equally to the diamictite clasts, we might expect the δ^{13}C of the clasts to be pulled to more negative values relative to the *in situ* carbonates since most of the samples in the *in situ* stratigraphy were extracted from carbonate horizons thicker than the diamictite clasts, but such a distribution is not observed.

There are several potential explanations for this apparent inconsistency. First, as discussed in the main text, samples that fall below the threshold d may or may not have had their carbon isotopic composition altered. And so, even though the majority of sampled diamictite clasts have a radius <0.2 m, the δ^{13}C of a significant proportion of these samples need not have been affected by secondary alteration. Second, it is possible that carbon is better buffered in the diamictite relative to the rest of the Tambien Group. Unless 100% of the diamictite's matrix was produced via scouring and redeposition of pre-Snowball Earth siliciclastics with associated organic matter, the matrix likely contains less low δ^{13}C organic carbon relative to the siliciclastic units of the underlying Tambien Group, given that organic productivity was suppressed during the Snowball Earth (Hoffman et al., 2017). The presence of extra-basinal clasts within the diamictite (see main text) suggests that at least some of the protolith was sourced from distal bedrock, and thus the organic component of the diamictite's matrix was likely diluted relative to undisturbed Tambien Group siliciclastics. Third, given that glacial erosion generates a bimodal sediment size distribution (fine grains from scouring and larger clasts from plucking) from the same rock, the

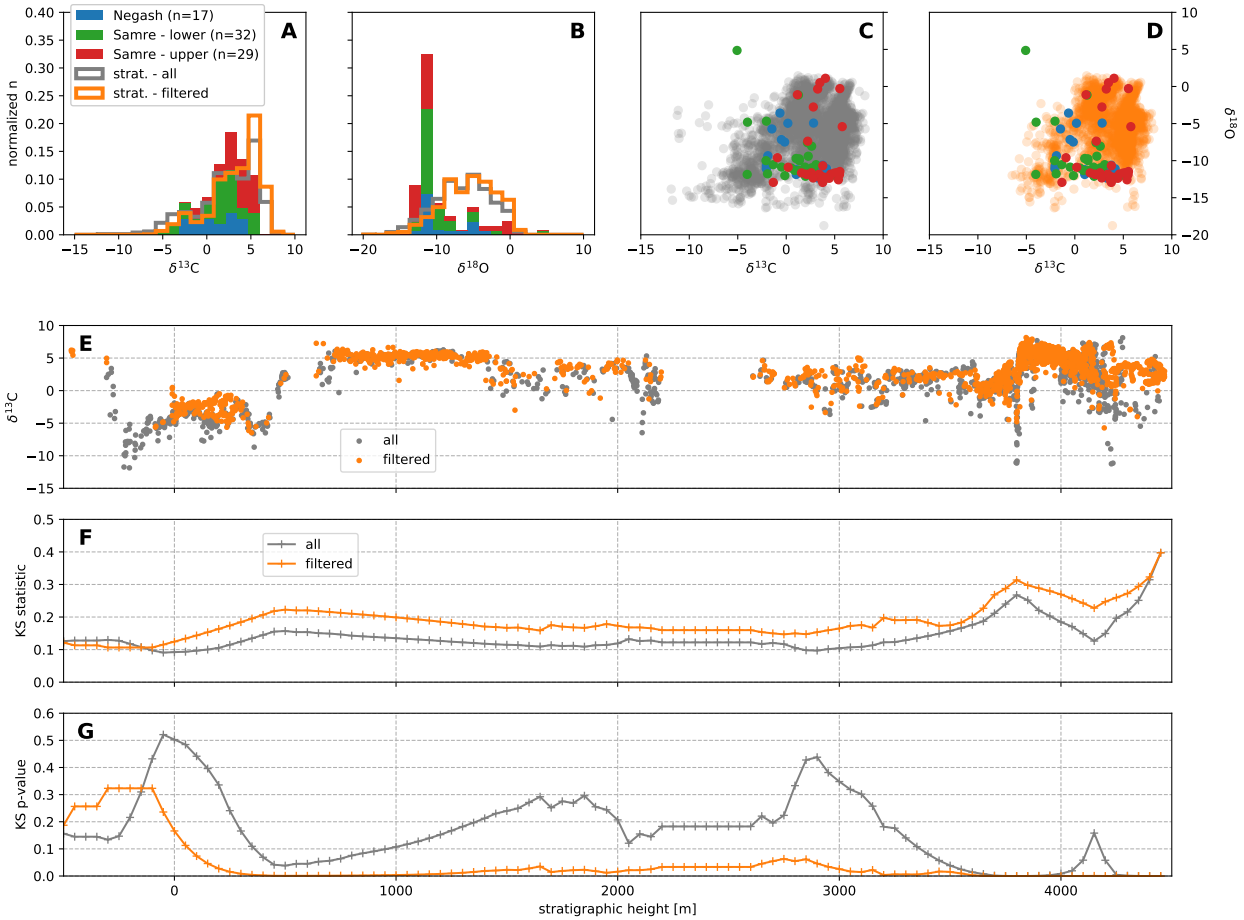

Figure DR3. **(A)** and **(B)** Histograms of δ^{13}C and δ^{18}O values of carbonate clasts within the diamictite of the Negash Formation of both the Negash Syncline and Samre Fold-Thrust Belt, compared to all *in situ* Tambien Group carbonate samples. Both filtered and unfiltered (all) versions of the *in situ* carbonate data are shown (see main text for a discussion of the filtering method). **(C)** and **(D)** Cross plots of δ^{13}C vs δ^{18}O for the clasts and *in situ* carbonate samples. **(E)** Filtered and unfiltered versions of the *in situ* carbonate δ^{13}C data against cumulative stratigraphic height. **(F)** Degree of correlation (as quantified by the Kolgomorov-Smirnov statistic) between the *in situ* carbonate δ^{13}C data with the carbonate clasts within the diamictite as samples below a given cumulative stratigraphic height (x-axis) are removed (i.e. the x-axis represents the depth of erosion). Low values suggest that the two datasets are drawn from the same distribution. See accompanying text for further details. **(G)** Kolgomorov-Smirnov statistic p-value. High values suggest that the two datasets are drawn from the same distribution.

sampled carbonate clasts in the diamictite are likely accompanied by fine carbonate sand from the same rock. This relatively carbonate-rich diamictite matrix would help to buffer the carbon

isotopic composition of diamictite clasts against changes in $\delta^{13}C$ in a way that siliciclastic units within the *in situ* Tambien Group stratigraphy would not be able to. Finally, it is possible that our sampling of clasts from the diamictite is not representative of the bulk population. The total number of diamictite clasts sampled (n = 78) is substantially smaller than the total number of samples from *in situ* Tambien Group carbonates (n = 3139). Furthermore, diamictite clasts were only sampled from three discrete stratigraphic horizons, which may have been more carbonate buffered relative to the rest of the diamictite.

$\delta^{18}O$ values of the diamictite clasts are distinctly different from the spread in values observed in the *in situ* stratigraphy, and cluster at ∼-12‰ (Fig. DR3B). This difference suggests that, unlike the carbon isotopic composition, the oxygen isotope composition of the carbonate clasts was significantly more overprinted following deposition of the diamictite than that of the *in situ* carbonates. This difference in post-depositional alteration likely arises from the fact that the carbonate clasts in the diamictite are embedded within a predominantly siliciclastic matrix and are therefore less carbonate buffered against altering fluids, whereas most of the samples in the *in situ* stratigraphy were extracted from carbonate horizons thicker than the diamictite clasts and are therefore more likely to be carbonate buffered. Since carbon is more rock-buffered against altering fluids than oxygen, the $\delta^{13}C$ of the clasts are more likely to preserve primary values.

Glacial erosion during the Sturtian Glaciation likely preferentially eroded the upper Tambien Group in most places instead of eroding all the way to the base of the Tambien Group. To assess how deep the bulk of glaciers eroded into Tambien Group stratigraphy, we divided the Tambien Group chemostratigraphic composite data collected from the *in situ* stratigraphy (Fig. DR3E) into several equal length (50 m) stratigraphic windows, and randomly selected the same number of samples from each of these windows. This Monte Carlo approach is necessary to avoid bias toward relatively heavily sampled intervals of the stratigraphy. We then quantified the similarity in distributions between the $\delta^{13}C$ of the Monte Carlo sampled *in situ* stratigraphy with that of the diamictite clasts using the two sample Kolmogorov-Smirnov (KS) statistic, which tests

whether two sets of samples are consistent with being drawn from the same distribution. Low KS statistics and high p-values suggest that the two samples are drawn from the same distribution. We then simulate shallower erosion by iteratively excluding the lowest of these stratigraphic windows and recalculating the KS statistic, moving up the stratigraphy (Fig. DR3F and G). In general, we find that the two distributions are closest when the 'erosion height' is close to the bottom of the Tambien Group (∼0 m in Fig. DR3F and G) and near the middle of the Tambien Group (∼2900 m). We also observe a distinct trough/peak near the top of the Tambien Group (∼4200 m), although the KS statistic/p-value is not as low/high as at the bottom or near the middle of the Tambien Group. Furthermore, the filtered version of the *in situ* carbonate δ^{13}C data (see main text) matches the clast data more poorly than all of the *in situ* carbonate δ^{13}C data, likely as a result of similar post-depositional alteration mechanisms operating throughout the entirety of the Tambien Group. Ultimately, this analysis illustrates the fact that a relatively large proportion of the diamictite clasts have relatively low δ^{13}C (<0‰), and thus the clast δ^{13}C distribution matches the *in situ* carbonate δ^{13}C distribution when the 'erosion height' is such that it includes a high proportion of samples within the Bitter Springs stage, the Didikama-Matheos excursion, and/or carbonate samples that have likely experienced secondary alteration pulling them to lower δ^{13}C values. Observations of the facies of clasts within the diamictite suggest that they were sourced predominantly from the Matheos and/or Mariam Bohkahko formations (see main text), and thus an 'erosion height' of ∼2900 m or ∼4200 m would be consistent with these facies. The KS statistic/p-value at these 'erosion heights' is low/high enough such that we cannot reject the null hypothesis that the diamictite clasts and the *in situ* carbonate samples from above these heights come from the same distribution. However, we note that erosion into the Mariam Bohkahko/Matheos formations is not observed locally where the diamictite is deposited. This observation requires that the clasts derive from carbonates time-equivalent to these formations deposited elsewhere in the basin, or from carbonates deposited in another basin within an Arabian-Nubian terrane.

Sample Proximity to Siliciclastic Units

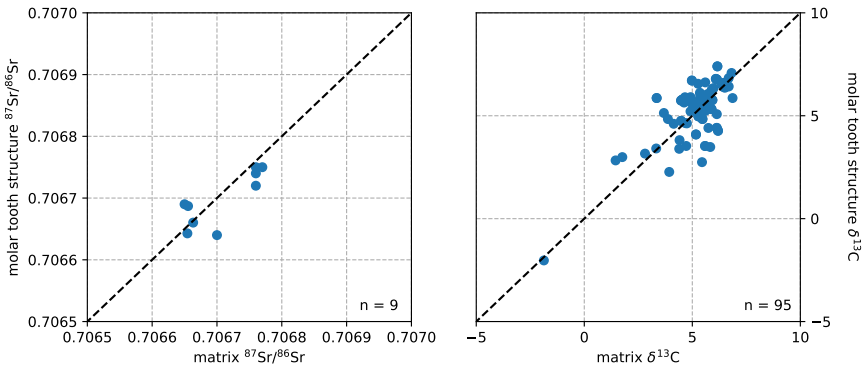

Figure DR4. Cross plots of carbonate matrix vs. adjacent molar tooth structure calcite $^{87}Sr/^{86}Sr$ and $\delta^{13}C$ from Tambien Group samples that meet the filtering thresholds for alteration (see main text). Dashed black lines are the 1:1 lines - samples that fall on these lines have identical isotopic composition between the matrix and molar tooth structure carbonate. The isotopic composition of the matrix is similar to that of adjacent molar tooth structures, and no systematic offsets can be identified.

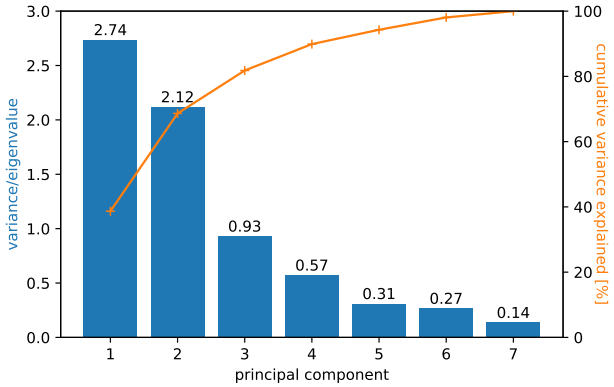

Figure DR5. Eigenvalues and cumulative variance explained for the 7 principal components in the principal components analysis (also known as a scree plot). Notably, the magnitude of the eigenvalues (and the percent variance explained) drops off sharply after the second principal component, indicating that the first two principal components capture the most significant sources of variance in our dataset.

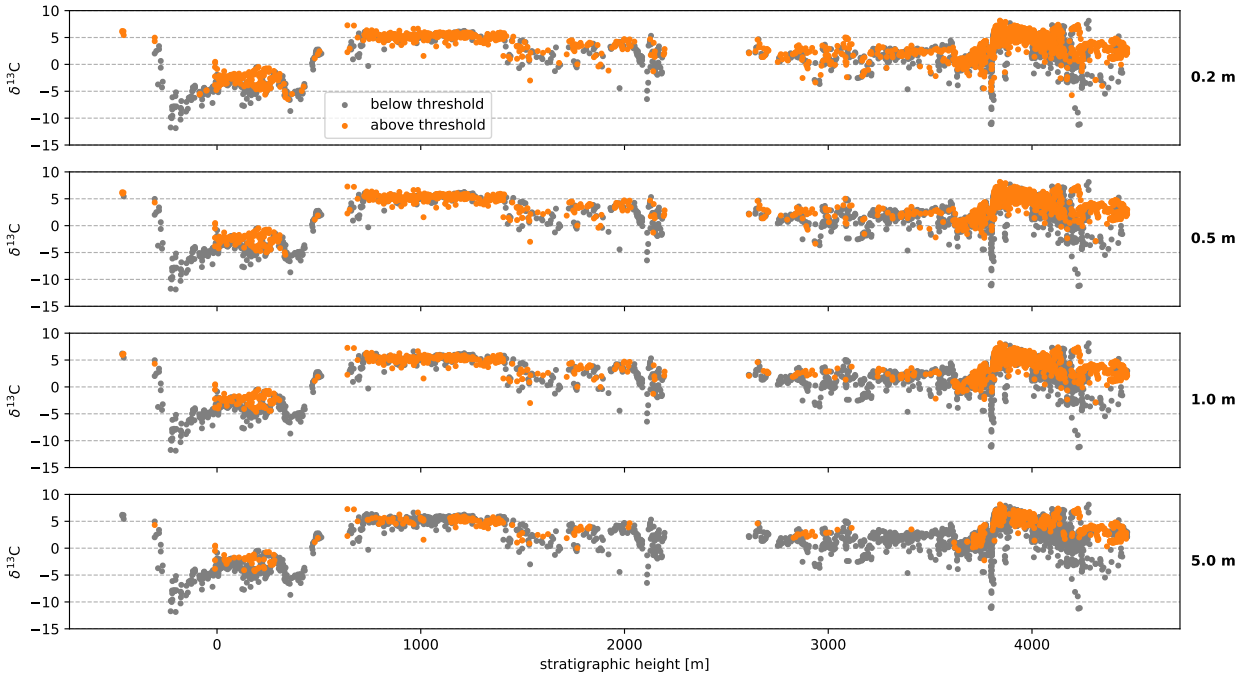

Figure DR6. Resulting composite chemostratigraphy of the Tambien Group as samples below a given d (shown on the right) are filtered out. Note that data that resolve the Didikama-Matheos excursion as well as the descent into and recovery out of the Bitter Springs stage are mostly removed under the $d = 0.2$ m threshold, and completely removed by $d = 0.5$ m.

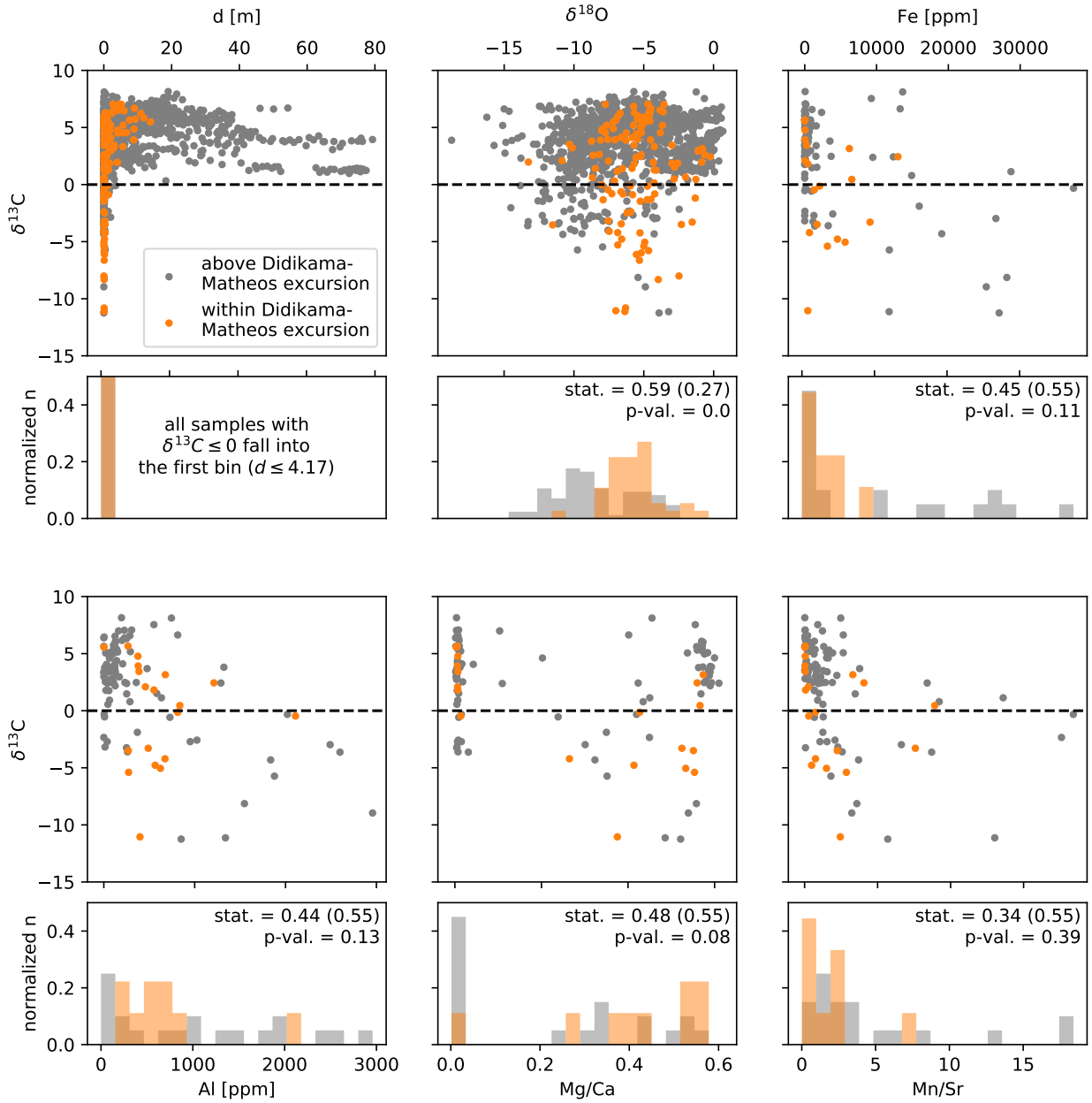

Figure DR7. Comparison of individual samples above the Didikama-Matheos excursion vs. samples within/adjacent to the Didikama-Matheos excursion. The normalized histograms under each scatter plot compare the distribution of samples with δ^{13}C $\leq$0‰ only. The 'stat.' and 'p-val.' refer to the Kolmogorov-Smirnov statistic and p-value respectively, with the value within the parentheses showing the critical Kolmogorov-Smirnov statistic for rejecting the null hypothesis (see text below).

As per conventions in statistics, the following discussion will use the term 'unit' to refer to an individual carbonate rock, and the term 'sample' to refer to a collection of 'units' from a population. Figure DR7 compares geochemical data of units above the Didikama-Matheos excursion to units within/adjacent to the Didikama-Matheos excursion. Units within the Didikama-Matheos excursion that record $\delta^{13}C \leq 0‰$ appear to exhibit lower Fe, Al, and Mn/Sr than units that record $\delta^{13}C \leq 0‰$ above the Didikama-Matheos excursion. This difference in distributions suggests that low $\delta^{13}C$ Didikama-Matheos excursion units have been less altered by the unbuffered fluids (see main text) than low $\delta^{13}C$ post-Didikama-Matheos excursion units, and thus provides support for the primary nature of the anomaly. To quantify this qualitative interpretation of the data, we compare the distributions of units with low $\delta^{13}C$ above the Didikama-Matheos excursion to units with low $\delta^{13}C$ within the Didikama-Matheos excursion by computing the two-sample Kolmogorov-Smirnov (KS) statistic. We also compute the critical KS statistic for rejecting the null hypothesis, which is given by $1.36\sqrt{\frac{N_1+N_2}{N_1N_2}}$, where N_1 and N_2 are the number of items in the two samples. If the computed KS statistic is above the critical KS statistic, or the p-value is below 0.05, we can reject the null hypothesis at the 95% confidence level that the two samples come from the same distribution. We find that the KS test yields ambiguous results for the Fe, Al, and Mn/Sr (Fig. DR7). For all three variables, the KS statistic is below the critical value, and the p-value is above 0.05. These results indicate that we cannot declare at the 95% confidence level that the two samples come from different distributions - instead, the test indicates that the samples may or may not come from the same distribution. However, the primary reason for this ambiguity is the small number of units used in the test. There are only 20 units with $\delta^{13}C \leq 0‰$ and element concentration data above the Didikama-Matheos excursion, and only 9 units with $\delta^{13}C \leq 0‰$ and element concentration within the Didikama-Matheos excursion, which results in a high critical KS statistic and thus a more 'difficult' test to achieve an unambiguous result in. Therefore, more element concentration data is required in order for the KS test to quantitatively reject the hypothesis at the 95% confidence level that units within the Didikama-Matheos excursion that record $\delta^{13}C \leq 0‰$ exhibit lower Fe,

296 Al, and Mn/Sr than units that record $\delta^{13}C \leq 0‰$ above the Didikama-Matheos excursion.

Sr Isotopes

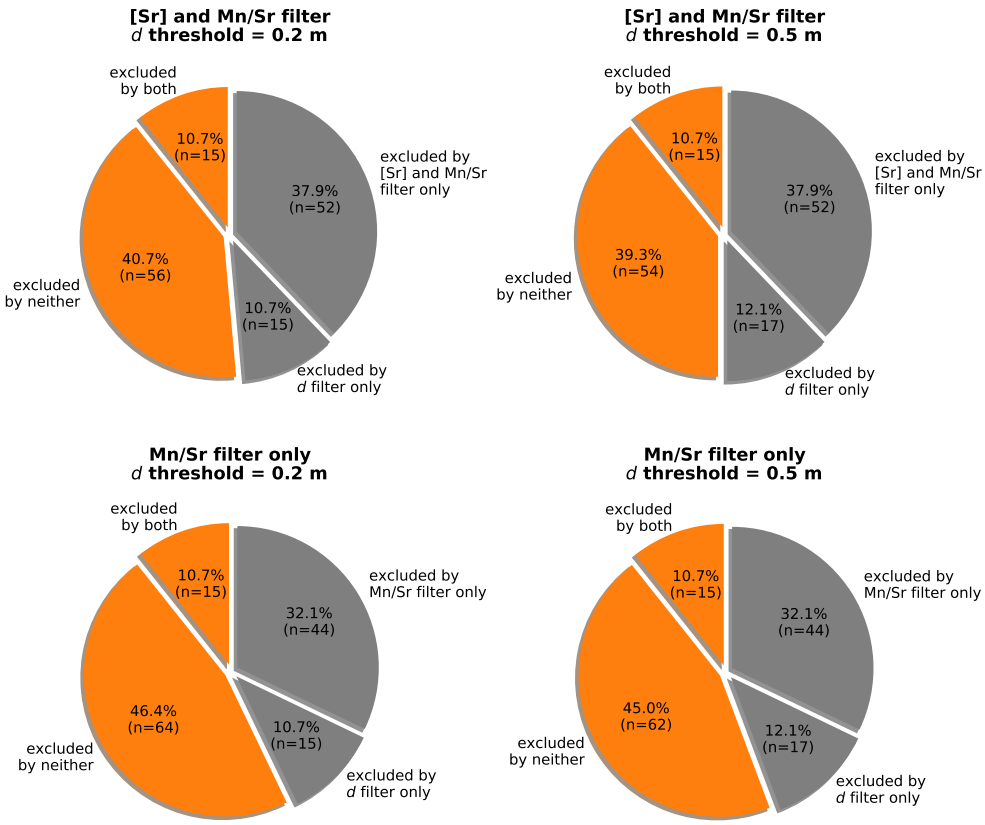

Figure DR8. Comparison of the application of the [Sr] and Mn/Sr filter and the filter based on distance to siliciclastics (d) to the $^{87}Sr/^{86}Sr$ data, for both $d = 0.2$ m and $d = 0.5$ m. Orange sectors denote classification agreement between the two filters, and grey sectors denote classification disagreement between the two filters. In the upper row, both the [Sr] and Mn/Sr thresholds are combined to filter samples. In the lower row, only the Mn/Sr threshold is used to filter samples.

Figure DR8 compares the application of the [Sr] and Mn/Sr filter and the filter based on distance to siliciclastics (d) to the $^{87}Sr/^{86}Sr$ data. When both the [Sr] and Mn/Sr thresholds are combined to filter samples (as in the main text), the [Sr] and Mn/Sr filter and the d filter only agree on classification for around half of the samples. This lack of agreement results from the fact that the principal components analysis used for the d filter (see main text) includes Mn/Sr, and not [Sr], as a variable in the analysis, since [Sr] in carbonates can vary considerably based on

factors other than secondary alteration (e.g. calcite vs. aragonite, Husson et al., 2015). Therefore, by using the Mn/Sr threshold only to filter samples, agreement between the Mn/Sr filter and the d filter improves. Still, considerable disagreement between the two filters remain, which highlights the limitations of the d filter as discussed in the main text. Namely, that in addition to filtering out samples that have been altered, it is a rather blunt filter and may also filter out samples that retain relatively pristine geochemistry.

Pre-Sturtian $^{87}Sr/^{86}Sr$ and the Drivers of Planetary Cooling

LIP Analysis

Table DR4 lists the large igneous provinces (LIPs) that were included in the LIP analysis in the main text. The extent of each LIP was traced in QGIS to generate shapefiles, which were then added to a paleogeographic model (Swanson-Hysell et al., 2019) to extract the paleolatitude of the LIPs. We note that the LIP polygons were drawn to include the full areal extent of all dykes, sills, and volcanics interpreted to be associated with each LIP, which may lead to an overestimate of the true emplacement extents, since subsurface intrusions could extend over a broader area than the surface volcanics. Where available, the paleogeographic model honors the paleomagnetic poles listed in Table DR4.

Global Weathering Model

The Python code used to develop the global weathering model can be found at: https://github.com/Swanson-Hysell-Group/2019_Tambien_Group. Table DR5 shows the variables and equations used in the global weathering model.

Table DR4. Large igneous provinces included in the analysis conducted in the main text.

Name	Craton	Emplacement Age [Ma]	Emplacement Area [Mkm^2]	Polygon Centroid Emplacement Latitude	Age Reference	Polygon Reference	Paleomagnetic Pole Reference
Mackenzie	Laurentia	1267	2.983	11.4	LeCheminant and Heaman (1989)	Ernst and Youbi (2017)	Buchan et al. (2000)
CSDG	Baltica	1255	0.145	-24	Söderlund et al. (2006)	Ernst and Youbi (2017)	Pisarevsky et al. (2014a)
Sudbury	Laurentia	1235	0.056	7.7	Dudas et al. (1994)	Shellnutt and MacRae (2012)	Palmer et al. (1977)
Marnda Moorn	SW. Australia	1210	0.598	65.2	Pisarevsky et al. (2014b)	Ernst and Youbi (2017)	Pisarevsky et al. (2014b)
Abitibi	Laurentia	1141	0.229	48.2	Krogh et al. (1987)	Ernst and Youbi (2017)	Ernst and Buchan (1993)
Umkondo	Kalahari	1109	1.846	0.8	Hanson et al. (2004)	Ernst and Youbi (2017)	Swanson-Hysell et al. (2015a)
Keweenawan	Laurentia	1109	0.414	41.9	Davis and Green (1997)	Ernst and Youbi (2017)	Swanson-Hysell et al. (2014)
SW Laurentia	Laurentia	1090	0.776	28.7	Weil et al. (2003)	Bright et al. (2014)	Weil et al. (2003)
Warakurna - 1	SW. + N. Australia	1070	0.757	38.6	Wingate et al. (2002)	Ernst and Youbi (2017)	Wingate et al. (2002)
Warakurna - 2	SW. + N. Australia	1070	0.444	41.9	Wingate et al. (2002)	Ernst and Youbi (2017)	Wingate et al. (2002)
Dashigou	N. China	925	0.663	3.9	Peng et al. (2011)	Pirajno (2013)	-
Gangil-Mayumbia	Congo	920	0.333	-52.3	Tack et al. (2001)	Ernst and Youbi (2017)	-
Willouran-Gairdner - 1	S. Australia	827	0.345	24.3	Wingate et al. (1998)	Ernst and Youbi (2017)	-
Willouran-Gairdner - 2	S. Australia	827	0.171	29.3	Wingate et al. (1998)	Ernst and Youbi (2017)	-
SWCUC - 1	S. China	821	0.914	68.6	Wang et al. (2016)	Ernst and Youbi (2017)	Li et al. (2004)
SWCUC - 2	S. China	821	0.411	65.6	Wang et al. (2016)	Ernst and Youbi (2017)	Li et al. (2004)
Gunbarrel - 1	Laurentia	780	0.21	-7	Harlan et al. (2003)	Ernst and Youbi (2017)	Park et al. (1989)
Gunbarrel - 2	Laurentia	780	0.34	4.2	Harlan et al. (2003)	Ernst and Youbi (2017)	Park et al. (1989)
Mundine Well	N. Australia	755	0.21	25.6	Wingate and Giddings (2000)	Ernst and Youbi (2017)	Wingate and Giddings (2000)
Irkutsk	Siberia	724	0.154	13.6	Ernst et al. (2016)	Ernst et al. (2016)	-
Franklin	Laurentia	720	2.231	-2.3	Denyszyn et al. (2009)	Ernst and Youbi (2017)	Denyszyn et al. (2009)

Notes:
LIPs >0.1 Mkm^2 from the compilation in (Ernst et al., 2008) were included in the LIP analysis in the main text. Some LIPs are comprised of two separate polygons (denoted by 1 and 2).

Table DR5. Variables used in the global weathering model.

Term	Value/Equation	Note
Subaerial		
$[Ca]_{carb}$	302300 ppm	(1)
$[Mg]_{carb}$	47000 ppm	(1)
$[Sr]_{carb}$	610 ppm	(1)
$[Ca]_{rad}$	23750 ppm	(2)
$[Mg]_{rad}$	12800 ppm	(2)
$[Sr]_{rad}$	310 ppm	(2)
$[Ca]_{juv}$	71600 ppm	(3)
$[Mg]_{juv}$	45500 ppm	(3)
$[Sr]_{juv}$	465 ppm	(3)
Hydrothermal		
$H_{Mg-clays}$	$k \cdot [Mg]$	-
k	-	(4)
$H_{Ca-basalt}$	$\alpha_{Mg/Ca} \cdot H_{Mg-clays}$	-
$\alpha_{Mg/Ca}$	1	(5)
$H_{^nSr-basalt}$	$\alpha_{Sr/Ca} \cdot H_{Ca-basalt}$	-
$\alpha_{Sr/Ca}$	0.0013	(6)
Precipitation		
$P_{Ca-carb}$	$W_{Mg-carb} + W_{Mg-rad} + W_{Mg-juv} - P_{Mg-carb} + W_{Ca-carb} + W_{Ca-rad} + W_{Ca-juv}$	(7)
$P_{Mg-carb}$	5×10^{10} mol/yr	(8)
$P_{Sr-carb}$	$(Sr/Ca)_{seawater} \cdot K_{Sr} \cdot P_{Ca-carb}$	-
K_{Sr}	0.2	(9)
$^{87}Sr/^{86}Sr$		
carbonate	0.70475	(10)
radiogenic	$BABI + (0.2783 \left(\frac{Rb}{Sr}\right)_m (9.3485 + BABI))(1 - e^{-2\times10^9\lambda}) +$ $10(0.2783 \left(\frac{Rb}{Sr}\right)_m (9.3485 + BABI))(1 - e^{-\lambda(t-2\times10^9)})$	(11)
juvenile	$BABI + (0.2783 \left(\frac{Rb}{Sr}\right)_m (9.3485 + BABI))(1 - e^{-\lambda t})$	(11)

Notes:
(1) from Turekian and Wedepohl (1961)
(2) from Wedepohl (1995)
(3) taking the mean of Turekian and Wedepohl (1961) and Taylor (1964)
(4) flux of H_2O in hydrothermal systems, estimated to achieve desired initial steady state, then varied
(5) assumes 1:1 stoichiometry between Mg and Ca during weathering of the ocean crust
(6) from Maloof et al. (2010), calculated assuming 200 ppm Sr and 10 wt% CaO
(7) calculated iteratively assuming carbonate minerals are the only Ca sink
(8) estimated to achieve desired initial steady state
(9) homogeneous distribution coefficient for Sr in calcite from Mucci and Morse (1983)
(10) seawater has roughly constant $^{87}Sr/^{86}Sr$ ~2-1 Ga (Shields and Veizer, 2002)
(11) these equations account of ^{87}Rb decay, where $BABI$ is the Basaltic Achondrite Best Initial ratio ($^{87}Sr/^{86}Sr$ =0.69897) from Papanastassiou and Wasserburg (1968), $\left(\frac{Rb}{Sr}\right)_m$ is Rb/Sr of the mantle (0.025), λ is the ^{87}Rb decay constant, and t is time since the origin of the Earth.

References

Aitken, J. D., 1981, Stratigraphy and sedimentology of the Upper Proterozoic Little Dal Group, Mackenzie Mountains, Northwest Territories: Mackenzie Mountains, Northwest Territories: Geological Survey of Canada, Paper, vol. 8110, pp. 47–81.

Asmerom, Y., Jacobsen, S. B., Knoll, A. H., Butterfield, N. J., and Swett, K., 1991, Strontium isotopic variations of Neoproterozoic seawater: implications for crustal evolution: Geochimica et Cosmochimica Acta, vol. 55, pp. 2883–2894, doi:10.1016/0016-7037(91)90453-C.

Bartley, J. K., Semikhatov, M. A., Kaufman, A. J., Knoll, A. H., Pope, M. C., and Jacobsen, S. B., 2001, Global events across the Mesoproterozoic-Neoproterozoic boundary: C and Sr isotopic evidence from Siberia: Precambrian Research, vol. 111, pp. 165–202, doi:10.1016/S0301-9268(01)00160-7.

Bold, U., Smith, E. F., Rooney, A. D., Bowring, S. A., Buchwaldt, R., Dudás, F. Ő., Ramezani, J., Crowley, J. L., Schrag, D. P., and Macdonald, F. A., 2016, Neoproterozoic stratigraphy of the Zavkhan terrane of Mongolia: the backbone for Cryogenian and early Ediacaran chemostratigraphic records: American Journal of Science, vol. 316, pp. 1–63, doi:10.2475/01.2016.01.

Brasier, M., McCarron, G., Tucker, R., Leather, J., Allen, P., and Shields, G., 2000, New U-Pb zircon dates for the Neoproterozoic Ghubrah glaciation and for the top of the Huqf Supergroup, Oman: Geology, vol. 28, pp. 175–178, doi:10.1130/0091-7613(2000)28⟨175:NUZDFT⟩2.0.CO;2.

Brasier, M. D., Shields, G., Kuleshov, V. N., and Zhegallo, E. A., 1996, Integrated chemo- and biostratigraphic calibration of early animal evolution: Neoproterozoic-early Cambrian of southwest Mongolia: Geological Magazine, vol. 133, pp. 445–485, doi:10.1017/S0016756800007603.

Bright, R. M., Amato, J. M., Denyszyn, S. W., and Ernst, R. E., 2014, U-Pb geochronology of 1.1 Ga diabase in the southwestern United States: testing models for the origin of a post-Grenville large igneous province: Lithosphere, vol. 6, pp. 135–156, doi:10.1130/L335.1.

Buchan, K. L., Mertanen, S., Park, R. G., Pesonen, L. J., Elming, S.-Å., Abrahamsen, N., and Bylund, G., 2000, Comparing the drift of Laurentia and Baltica in the Proterozoic: the importance of key palaeomagnetic poles: Tectonophysics, vol. 319, pp. 167–198, doi:10.1016/S0040-1951(00)00032-9.

Calver, C. R., Crowley, J. L., Wingate, M. T. D., Evans, D. A. D., Raub, T. D., and Schmitz, M. D., 2013, Globally synchronous Marinoan deglaciation indicated by U-Pb geochronology of the Cottons Breccia, Tasmania, Australia: Geology, vol. 41, pp. 1127–1130, doi:10.1130/G34568.1.

Condon, D., Zhu, M., Bowring, S., Wang, W., Yang, A., and Jin, Y., 2005, U-Pb ages from the Neoproterozoic Doushantuo Formation, China: Science, vol. 308, pp. 95–98, doi:10.1126/science.1107765.

Cox, G. M., Halverson, G. P., Stevenson, R. K., Vokaty, M., Poirier, A., Kunzmann, M., Li, Z.-X., Denyszyn, S. W., Strauss, J. V., and Macdonald, F. A., 2016, Continental flood basalt weathering as a trigger for Neoproterozoic Snowball Earth: Earth and Planetary Science Letters, vol. 446, pp. 89–99, doi:10.1016/j.epsl.2016.04.016.

Cox, G. M., Isakson, V., Hoffman, P. F., Gernon, T. M., Schmitz, M. D., Shahin, S., Collins, A. S., Preiss, W., Blades, M. L., Mitchell, R. N., and et al., 2018, South Australian U-Pb zircon (CA-ID-TIMS) age supports globally synchronous Sturtian deglaciation: Precambrian Research, vol. 315, pp. 257–263, doi:10.1016/j.precamres.2018.07.007.

Davis, D. W. and Green, J. C., 1997, Geochronology of the North American Midcontinent rift in western Lake Superior and implications for its geodynamic evolution: Canadian Journal of Earth Sciences, vol. 34, pp. 476–488, doi:10.1139/e17-039.

Denyszyn, S. W., Halls, H. C., Davis, D. W., and Evans, D. A., 2009, Paleomagnetism and U-Pb geochronology of Franklin dykes in High Arctic Canada and Greenland: a revised age and paleomagnetic pole constraining block rotations in the Nares Strait region: Canadian Journal of Earth Sciences, vol. 46, pp. 689–705, doi:10.1139/E09-042.

Dudas, F. O., Davidson, A., and Bethune, K. M., 1994, Age of the Sudbury diabase dykes and their metamorphism in the Grenville Province, Ontario: *In* Radiogenic ace and isotopic studies, Geological Survey of Canada, pp. 97–106.

Ernst, R. E. and Buchan, K. L., 1993, Paleomagnetism of the Abitibi dyke swarm, southern Superior Province, and implications for the Logan Loop: Canadian Journal of Earth Sciences, vol. 30, pp. 1886–1897, doi:10.1139/e93-167.

Ernst, R. E., Hamilton, M. A., Söderlund, U., Hanes, J. A., Gladkochub, D. P., Okrugin, A. V., Kolotilina, T., Mekhonoshin, A. S., Bleeker, W., LeCheminant, A. N., Buchan, K. L., Chamberlain, K. R., and Didenko, A. N., 2016, Long-lived connection between southern Siberia and northern Laurentia in the Proterozoic: Nature Geoscience, vol. 9, pp. 464–469, doi:10.1038/ngeo2700.

Ernst, R. E., Wingate, M. T. D., Buchan, K. L., and Li, Z. X., 2008, Global record of 1600-700 ma Large Igneous Provinces (LIPs): implications for the reconstruction of the proposed Nuna (Columbia) and Rodinia supercontinents: Precambrian Research, vol. 160, pp. 159–178, doi:10.1016/j.precamres.2007.04.019.

Ernst, R. E. and Youbi, N., 2017, How large igneous provinces affect global climate, sometimes cause mass extinctions, and represent natural markers in the geological record: Palaeogeography, Palaeoclimatology, Palaeoecology, vol. 478, pp. 30–52, doi:10.1016/j.palaeo.2017.03.014.

Gallet, Y., Pavlov, V., Halverson, G., and Hulot, G., 2012, Toward constraining the long-term reversing behavior of the geodynamo: A new "Maya" superchron 1 billion years ago from the magnetostratigraphy of the Kartochka Formation (southwestern Siberia): Earth and Planetary Science Letters, vol. 339-340, pp. 117–126, doi:10.1016/j.epsl.2012.04.049.

399 Halverson, G. P., 2006, A Neoproterozoic Chronology, Springer Netherlands, Dordrecht, pp.
400 231–271: doi:10.1007/1-4020-5202-28.

401 Halverson, G. P., Dudás, F. Ö., Maloof, A. C., and Bowring, S. A., 2007a, Evolution of the
402 $^{87}Sr/^{86}Sr$ composition of Neoproterozoic seawater: Palaeogeography, Palaeoclimatology,
403 Palaeoecology, vol. 256, pp. 103–129, doi:10.1016/j.palaeo.2007.02.028.

404 Halverson, G. P., Hoffman, P. F., Schrag, D. P., Maloof, A. C., and Rice, A. H. N., 2005, Toward
405 a Neoproterozoic composite carbon-isotope record: GSA Bulletin, vol. 117, pp. 1181–1207,
406 doi:10.1130/B25630.1.

407 Halverson, G. P., Maloof, A. C., and Hoffman, P. F., 2004, The Marinoan glaciation
408 (Neoproterozoic) in northeast Svalbard: Basin Research, vol. 16, pp. 297–324,
409 doi:10.1111/j.1365-2117.2004.00234.x.

410 Halverson, G. P., Maloof, A. C., Schrag, D. P., Dudás, F. Ö., and Hurtgen, M., 2007b,
411 Stratigraphy and geochemistry of a ca 800 Ma negative carbon isotope interval in northeastern
412 Svalbard: Chemical Geology, vol. 237, pp. 5–27, doi:10.1016/j.chemgeo.2006.06.013.

413 Hanson, R. E., Crowley, J. L., Bowring, S. A., Ramezani, J., Gose, W. A., Dalziel, I. W. D.,
414 Pancake, J. A., Seidel, E. K., Blenkinsop, T. G., and Mukwakwami, J., 2004, Coeval large-scale
415 magmatism in the Kalahari and Laurentian cratons during Rodinia assembly: Science, vol. 304,
416 pp. 1126–1129, doi:10.1126/science.1096329.

417 Harlan, S. S., Heaman, L., LeCheminant, A. N., and Premo, W. R., 2003, Gunbarrel mafic
418 magmatic event: A key 780 Ma time marker for Rodinia plate reconstructions: Geology,
419 vol. 31, pp. 1053–1056, doi:10.1130/G19944.1.

420 Hoffman, P. F., Abbot, D. S., Ashkenazy, Y., Benn, D. I., Brocks, J. J., Cohen, P. A., Cox, G. M.,
421 Creveling, J. R., Donnadieu, Y., Erwin, D. H., Fairchild, I. J., Ferreira, D., Goodman, J. C.,
422 Halverson, G. P., Jansen, M. F., Le Hir, G., Love, G. D., Macdonald, F. A., Maloof, A. C.,
423 Partin, C. A., Ramstein, G., Rose, B. E. J., Rose, C. V., Sadler, P. M., Tziperman, E., Voigt,
424 A., and Warren, S. G., 2017, Snowball Earth climate dynamics and Cryogenian
425 geology-geobiology: Science Advances, vol. 3, doi:10.1126/sciadv.1600983.

426 Hoffmann, K.-H., Condon, D. ., Bowring, S. A., and Crowley, J. L., 2004, U-Pb zircon date from
427 the Neoproterozoic Ghaub Formation, Namibia: Constraints on Marinoan glaciation: Geology,
428 vol. 32, pp. 817–820, doi:10.1130/G20519.1.

429 Husson, J. M., Higgins, J. A., Maloof, A. C., and Schoene, B., 2015, Ca and Mg isotope
430 constraints on the origin of Earth's deepest C excursion: Geochimica et Cosmochimica Acta,
431 vol. 160, pp. 243–266, doi:10.1016/j.gca.2015.03.012.

432 Jaffey, A. H., Flynn, K. F., Glendenin, L. E., Bentley, W. C., and Essling, A. M., 1971, Precision
433 measurement of half-lives and specific activities of ^{235}U and ^{238}U: Phys. Rev. C, vol. 4, pp.
434 1889–1906, doi:10.1103/PhysRevC.4.1889.

435 Jones, D. S., Maloof, A. C., Hurtgen, M. T., Rainbird, R. H., and Schrag, D. P., 2010, Regional
436 and global chemostratigraphic correlation of the early Neoproterozoic Shaler Supergroup,
437 Victoria Island, Northwestern Canada: Precambrian Research, vol. 181, pp. 43–63,
438 doi:10.1016/j.precamres.2010.05.012.

439 Kendall, B., Creaser, R. A., and Selby, D., 2006, Re-Os geochronology of postglacial black shales
440 in Australia: Constraints on the timing of "Sturtian" glaciation: Geology, vol. 34, pp. 729–732,
441 doi:10.1130/G22775.1.

442 Krogh, T. E., Corfu, F., Davis, D. W., Dunning, G. R., Heaman, L. M., Kamo, S. L., Machado,
443 N., Greenough, J. D., and Nakamura, E., 1987, Precise U-Pb isotopic ages of diabase dykes and
444 mafic to ultra mafic rocks using trace amounts of baddeleyite and zircon: *In* Halls, H. C. and
445 Fahrig, W. F., eds., Mafic dyke swarms, Geological Association of Canada, pp. 147–152.

446 Kuznetsov, A. B., Semikhatov, M. A., Maslov, A. V., Gorokhov, I. M., Prasolov, E. M.,
447 Krupenin, M. T., and Kislova, I. V., 2006, New data on Sr-and C-isotopic chemostratigraphy of
448 the Upper Riphean type section (Southern Urals): Stratigraphy and Geological Correlation,
449 vol. 14, pp. 602–628, doi:10.1134/S0869593806060025.

450 LeCheminant, A. N. and Heaman, L. M., 1989, Mackenzie igneous events, Canada: Middle
451 Proterozoic hotspot magmatism associated with ocean opening: Earth and Planetary Science
452 Letters, vol. 96, pp. 38–48, doi:10.1016/0012-821X(89)90122-2.

453 Li, Z. X., Evans, D. A. D., and Zhang, S., 2004, A 90° spin on Rodinia: possible causal links
454 between the Neoproterozoic supercontinent, superplume, true polar wander and low-latitude
455 glaciation: Earth and Planetary Science Letters, vol. 220, pp. 409–421,
456 doi:10.1016/S0012-821X(04)00064-0.

457 Macdonald, F. A., Schmitz, M. D., Crowley, J. L., Roots, C. F., Jones, D. S., Maloof, A. C.,
458 Strauss, J. V., Cohen, P. A., Johnston, D. T., and Schrag, D. P., 2010, Calibrating the
459 Cryogenian: Science, vol. 327, pp. 1241–1243, doi:10.1126/science.1183325.

460 MacLennan, S. A., Park, Y., Swanson-Hysell, N. L., Maloof, A. C., Schoene, B., Gebreslassie, M.,
461 Antilla, E., Tesema, T., Alene, M., and Haileab, B., 2018, The arc of the Snowball: U-Pb dates
462 constrain the Islay anomaly and the initiation of the Sturtian glaciation: Geology, vol. 46, pp.
463 539–542, doi:10.1130/G40171.1.

464 Maloof, A. C., Halverson, G. P., Kirschvink, J. L., Schrag, D. P., Weiss, B. P., and Hoffman,
465 P. F., 2006, Combined paleomagnetic, isotopic, and stratigraphic evidence for true polar
466 wander from the Neoproterozoic Akademikerbreen Group, Svalbard, Norway: GSA Bulletin,
467 vol. 118, pp. 1099–1124, doi:10.1130/B25892.1.

468 Maloof, A. C., Porter, S. M., Moore, J. L., Dudás, F. Ö., Bowring, S. A., Higgins, J. A., Fike,
469 D. A., and Eddy, M. P., 2010, The earliest Cambrian record of animals and ocean geochemical
470 change: Geological Society of America Bulletin, vol. 122, pp. 1731–1774, doi:10.1130/B30346.1.

Miller, N. R., Stern, R. J., Avigad, D., Beyth, M., and Schilman, B., 2009, Cryogenian slate-carbonate sequences of the Tambien Group, Northern Ethiopia (I): Pre-"Sturtian" chemostratigraphy and regional correlations: Precambrian Research, vol. 170, pp. 129–156, doi:10.1016/j.precamres.2008.12.004.

Mucci, A. and Morse, J. W., 1983, The incorporation of Mg^{2+} and Sr^{2+} into calcite overgrowths: influences of growth rate and solution composition: Geochimica et Cosmochimica Acta, vol. 47, pp. 217–233, doi:10.1016/0016-7037(83)90135-7.

Palmer, H. C., Merz, B. A., and Hayatsu, A., 1977, The Sudbury dikes of the Grenville Front region: paleomagnetism, petrochemistry, and K-Ar age studies: Canadian Journal of Earth Sciences, vol. 14, pp. 1867–1887, doi:10.1139/e77-158.

Papanastassiou, D. and Wasserburg, G., 1968, Initial strontium isotopic abundances and the resolution of small time differences in the formation of planetary objects: Earth and Planetary Science Letters, vol. 5, pp. 361–376, doi:10.1016/S0012-821X(68)80066-4.

Park, J. K., Norris, D. K., and Larochelle, A., 1989, Paleomagnetism and the origin of the Mackenzie Arc of northwestern Canada: Canadian Journal of Earth Sciences, vol. 26, pp. 2194–2203, doi:10.1139/e89-186.

Peng, P., Bleeker, W., Ernst, R. E., Söderlund, U., and McNicoll, V., 2011, U-Pb baddeleyite ages, distribution and geochemistry of 925Ma mafic dykes and 900Ma sills in the North China craton: Evidence for a Neoproterozoic mantle plume: Lithos, vol. 127, pp. 210–221, doi:10.1016/j.lithos.2011.08.018.

Pirajno, F., 2013, Large Igneous Provinces (Xiong'er, Dashigou, 827 Ma Event, Tarim, Emeishan) and the Yanshanian tectono-thermal Event of Eastern China, Springer Netherlands, Dordrecht, pp. 547–638: doi:10.1007/978-94-007-4444-8-7.

Pisarevsky, S. A., Elming, S.-Å., Pesonen, L. J., and Li, Z.-X., 2014a, Mesoproterozoic paleogeography: Supercontinent and beyond: Precambrian Research, vol. 244, pp. 207–225, doi:10.1016/j.precamres.2013.05.014.

Pisarevsky, S. A., Wingate, M. T. D., Li, Z.-X., Wang, X.-C., Tohver, E., and Kirkland, C. L., 2014b, Age and paleomagnetism of the 1210Ma Gnowangerup-Fraser dyke swarm, Western Australia, and implications for late Mesoproterozoic paleogeography: Precambrian Research, vol. 246, pp. 1–15, doi:10.1016/j.precamres.2014.02.011.

Rooney, A. D., Macdonald, F. A., Strauss, J. V., Dudás, F. Ö., Hallmann, C., and Selby, D., 2014, Re-Os geochronology and coupled Os-Sr isotope constraints on the Sturtian snowball Earth: Proceedings of the National Academy of Sciences, vol. 111, pp. 51–56, doi:10.1073/pnas.1317266110.

Rooney, A. D., Strauss, J. V., Brandon, A. D., and Macdonald, F. A., 2015, A Cryogenian chronology: Two long-lasting synchronous Neoproterozoic glaciations: Geology, vol. 43, pp. 459–462, doi:10.1130/G36511.1.

508 Rose, C. V., Swanson-Hysell, N. L., Husson, J. M., Poppick, L. N., Cottle, J. M., Schoene, B., and
509 Maloof, A. C., 2012, Constraints on the origin and relative timing of the Trezona $\delta^{13}C$ anomaly
510 below the end-Cryogenian glaciation: Earth and Planetary Science Letters, vol. 319-320, pp.
511 241–250, doi:10.1016/j.epsl.2011.12.027.

512 Sawaki, Y., Kawai, T., Shibuya, T., Tahata, M., Omori, S., Komiya, T., Yoshida, N., Hirata, T.,
513 Ohno, T., Windley, B. F., and Maruyama, S., 2010, $^{87}Sr/^{86}Sr$ chemostratigraphy of
514 Neoproterozoic Dalradian carbonates below the Port Askaig Glaciogenic Formation, Scotland:
515 Precambrian Research, vol. 179, pp. 150–164, doi:10.1016/j.precamres.2010.02.021.

516 Shellnutt, J. G. and MacRae, N. D., 2012, Petrogenesis of the Mesoproterozoic (1.23 Ga) Sudbury
517 dyke swarm and its questionable relationship to plate separation: International Journal of
518 Earth Sciences, vol. 101, pp. 3–23, doi:10.1007/s00531-010-0636-9.

519 Shields, G. and Veizer, J., 2002, Precambrian marine carbonate isotope database: Version 1.1:
520 Geochemistry, Geophysics, Geosystems, vol. 3, pp. 1 of 12–12 of 12, doi:10.1029/2001GC000266.

521 Söderlund, U., Elming, S.-Å., Ernst, R. E., and Schissel, D., 2006, The Central Scandinavian
522 Dolerite Group-protracted hotspot activity or back-arc magmatism?: Constraints from U-Pb
523 baddeleyite geochronology and Hf isotopic data: Precambrian Research, vol. 150, pp. 136–152,
524 doi:10.1016/j.precamres.2006.07.004.

525 Swanson-Hysell, N. L., Kilian, T. M., and Hanson, R. E., 2015a, A new grand mean
526 palaeomagnetic pole for the 1.11 Ga Umkondo large igneous province with implications for
527 palaeogeography and the geomagnetic field: Geophysical Journal International, vol. 203, pp.
528 2237–2247, doi:10.1093/gji/ggv402.

529 Swanson-Hysell, N. L., Maloof, A. C., Condon, D. J., Jenkin, G. R., Alene, M., Tremblay, M. M.,
530 Tesema, T., Rooney, A. D., and Haileab, B., 2015b, Stratigraphy and geochronology of the
531 Tambien Group, Ethiopia: evidence for globally synchronous carbon isotope change in the
532 Neoproterozoic: Geology, vol. 43, pp. 323–326, doi:10.1130/G36347.1.

533 Swanson-Hysell, N. L., Ramezani, J., Fairchild, L. M., and Rose, I. R., 2019, Failed rifting and
534 fast drifting: Midcontinent Rift development, Laurentia's rapid motion and the driver of
535 Grenvillian orogenesis: GSA Bulletin, vol. 131, pp. 913–940, doi:10.1130/b31944.1.

536 Swanson-Hysell, N. L., Rose, C. V., Calmet, C. C., Halverson, G. P., Hurtgen, M. T., and Maloof,
537 A. C., 2010, Cryogenian glaciation and the onset of carbon-isotope decoupling: Science, vol.
538 328, pp. 608–611, doi:10.1126/science.1184508.

539 Swanson-Hysell, N. L., Vaughan, A. A., Mustain, M. R., and Asp, K. E., 2014, Confirmation of
540 progressive plate motion during the Midcontinent Rift's early magmatic stage from the Osler
541 Volcanic Group, Ontario, Canada: Geochemistry, Geophysics, Geosystems, vol. 15, pp.
542 2039–2047, doi:10.1002/2013GC005180.

543 Tack, L., Wingate, M. T. D., Liégeois, J.-P., Fernandez-Alonso, M., and Deblond, A., 2001, Early
544 Neoproterozoic magmatism (1000-910 Ma) of the Zadinian and Mayumbian Groups

(Bas-Congo): onset of Rodinia rifting at the western edge of the Congo craton: Precambrian Research, vol. 110, pp. 277–306, doi:10.1016/S0301-9268(01)00192-9.

Taylor, S. R., 1964, Abundance of chemical elements in the continental crust: a new table: Geochimica et Cosmochimica Acta, vol. 28, pp. 1273–1285, doi:10.1016/0016-7037(64)90129-2.

Turekian, K. K. and Wedepohl, K. H., 1961, Distribution of the elements in some major units of the Earth's crust: Geological Society of America Bulletin, vol. 72, pp. 175–192, doi:10.1130/0016-7606(1961)72[175:DOTEIS]2.0.CO;2.

Wang, T., Zhang, S., and Ramezani, J., 2016, Age recalibration of the Xiaofeng dykes, South China, and its implications for true polar wander at ∼820 Ma: Acta Geologica Sinica - English Edition, vol. 90, p. 47, doi:10.1111/1755-6724.12878.

Wedepohl, K. H., 1995, The composition of the continental crust: Geochimica et Cosmochimica Acta, vol. 59, pp. 1217–1232, doi:10.1016/0016-7037(95)00038-2.

Weil, A. B., Geissman, J. W., Heizler, M., and der Voo, R. V., 2003, Paleomagnetism of Middle Proterozoic mafic intrusions and Upper Proterozoic (Nankoweap) red beds from the Lower Grand Canyon Supergroup, Arizona: Tectonophysics, vol. 375, pp. 199–220, doi:10.1016/S0040-1951(03)00339-1, orogenic Belts, Regional and Global Tectonics: A Memorial Volume to Chris McAulay Powell.

Wingate, M. T., Campbell, I. H., Compston, W., and Gibson, G. M., 1998, Ion microprobe U-Pb ages for Neoproterozoic basaltic magmatism in south-central Australia and implications for the breakup of Rodinia: Precambrian Research, vol. 87, pp. 135–159, doi:10.1016/S0301-9268(97)00072-7.

Wingate, M. T. D. and Giddings, J. W., 2000, Age and palaeomagnetism of the Mundine Well dyke swarm, Western Australia: implications for an Australia–Laurentia connection at 755 Ma: Precambrian Research, vol. 100, pp. 335–357, doi:10.1016/S0301-9268(99)00080-7.

Wingate, M. T. D., Pisarevsky, S. A., and Evans, D. A. D., 2002, Rodinia connections between Australia and Laurentia: no SWEAT, no AUSWUS?: Terra Nova, vol. 14, pp. 121–128, doi:10.1046/j.1365-3121.2002.00401.x.

Zhang, S., Jiang, G., and Han, Y., 2008, The age of the Nantuo Formation and Nantuo glaciation in South China: Terra Nova, vol. 20, pp. 289–294, doi:10.1111/j.1365-3121.2008.00819.x.

Zhou, C., Tucker, R., Xiao, S., Peng, Z., Yuan, X., and Chen, Z., 2004, New constraints on the ages of Neoproterozoic glaciations in south China: Geology, vol. 32, pp. 437–440, doi:10.1130/G20286.1.